Lanthanum fluoride nanoparticles for radiosensitization of tumors

Konstantin Kudinov[1], Devesh Bekah[2], Daniel Cooper[2], Sathvik Shastry[1], Colin Hill[3], Stephen Bradforth[1], Jay Nadeau[1,4]

[1] Department of Chemistry, University of Southern California, 920 Bloom Walk, Los Angeles, CA 90089 USA
[2] Department of Biomedical Engineering, McGill University, Montreal, QC H3A 2B4 Canada
[3] Department of Radiation Oncology, University of Southern California, Los Angeles, CA 90033 USA
[4]GALCIT, California Institute of Technology 1200 E. California Blvd. Pasadena, CA 91125. USA

ABSTRACT

Dense inorganic nanoparticles have recently been identified as promising radiosensitizers. In addition to dose enhancement through increased attenuation of ionizing radiation relative to biological tissue, scintillating nanoparticles can transfer energy to coupled photosensitizers to amplify production of reactive oxygen species, as well as provide UV-visible emission for optical imaging. Lanthanum fluoride is a transparent material that is easily prepared as nanocrystals, and which can provide radioluminescence at a number of wavelengths through simple substitution of lanthanum ions with other luminescent lanthanides. We have prepared lanthanum fluoride nanoparticles doped with cerium, terbium, or both, that have good spectral overlap with chlorin e6 or Rose Bengal photosensitizer molecules. We have also developed a strategy for stable conjugation of the photosensitizers to the nanoparticle surface, allowing for high energy transfer efficiencies on a per molecule basis. Additionally, we have succeeded in making our conjugates colloidally stable under physiological conditions. Here we present our latest results, using nanoparticles and nanoparticle-photosensitizer conjugates to demonstrate radiation dose enhancement in B16 melanoma cells. The effects of nanoparticle treatment prior to 250 kVp x-ray irradiation were investigated through clonogenic survival assays and cell cycle analysis. Using a custom apparatus, we have also observed scintillation of the nanoparticles and conjugates under the same conditions that the cell samples are irradiated.

Keywords:

Photodynamic therapy, radiation therapy, scintillation, radioluminescence, fluorescence lifetimes, energy transfer

1. INTRODUCTION

Nanoparticles with high atomic numbers, for example gold [1] and bismuth [2], are promising low-toxicity agents that can amplify the effective dose of ionizing radiation in a cell in which they are present. If successfully targeted to cancer cells, such nanoparticles could reduce the needed dose of therapeutic radiation or make a standard dose more effective against radiation-resistant cancers. This is especially relevant to lower-energy radiation sources such as brachytherapy, since the photoelectric effect is the primary mode of action at these energies [3] [4].

Although a large number of theoretical, *in vitro* and *in vivo* studies have confirmed this mechanism, there are still no clinical trials of Au-nanoparticle enhanced radiation therapy[5] [6] [7]. The primary obstacle is the large fraction of metal required in the cell for a substantial dose enhancement, with resulting difficulties in targeting and concerns about toxicity. Depending upon their shape and size, nanoparticles distribute to the spleen, liver, and/or kidneys, and may cause damage to these organs as well as potentially to the heart [8] [9] [10, 11].

Photodynamic therapy (PDT) is an alternative to radiation therapy that results in fewer side effects, better healing, and less damage to surrounding normal tissue. The mechanism of action of PDT is generation of singlet oxygen by a photosensitizing dye that has been allowed to accumulate in inflamed or malignant tissue. An external light source excites the dye once optimal accumulation has occurred (usually several days after injection). Because of the short radius of action of singlet oxygen, only localized cell damage takes place. Unfortunately, PDT is limited to cancers that are unpigmented, superficial, and accessible by a light source [12-14]. If the photosensitizer could be excited through deeper, pigmented tissue, the advantages of PDT could be extended to deeper lesions.

Colloidal Nanoparticles for Biomedical Applications XI, edited by Wolfgang J. Parak, Marek Osinski, Xing-Jie Liang
Proc. of SPIE Vol. 9722, 97220V · © 2016 SPIE · CCC code: 0277-786X/16/$18 · doi: 10.1117/12.2213374

If ionizing radiation could be used to excite a photosensitizer, the problem of penetration of the excitation light would be eliminated. While some dyes excite directly with x-rays or other therapeutic radiation, most do not. The most general approach to the problem is therefore to conjugate a dye used in photodynamic therapy to a nanoparticle that emits light under radioexcitation (scintillates) [15]. As with other types of energy transfer, the absorption spectrum of the photosensitizer dye must overlap with the emission spectrum of the nanoparticle. A few studies on this approach have been published, but the problem is complicated by the lack of biologically stable nanoscintillators [16, 17]. Nanoparticle aggregation must be minimized and the ligand chosen so that it is not displaced by inorganic salts or organic molecules present in the solutions used. In addition, the ligand has to contain a functional group that permits covalent attachment of photosensitizers to the nanoparticle. Previous work in our group has shown that the bisphosphonate alendronate satisfies most of these requirements [18], but nanoparticles coated with alendronate alone require conditions too acidic for biological applications (pH < 4).

Here we report alendronate-PEG capped lanthanum fluoride (LaF_3) nanoparticles doped with cerium (Ce^{3+}) and/or terbium (Tb^{3+}). The particles are stable in cell culture media. The emission spectrum of Ce^{3+} overlaps with the blue Soret band of most photosensitizers. Tb^{3+} has a strong emission peak at 542 nm, which overlaps with the absorption spectrum of the photosensitizer rose bengal (RB). We show energy transfer to the photosensitizers by steady-state and time-resolved emission spectroscopy, and demonstrate that the particles emit under x-ray excitation using therapeutic energies and dose rates.

2. MATERIALS AND METHODS

2.1 Particle synthesis

Lanthanum (III) nitrate hexahydrate (99.999%), citric acid (ACS, ≥99.5%), 6-bromohexanoic acid (97%), 1-Ethyl-3-(3-dimethylaminopropyl)carbodiimide (EDC) and ammonium fluoride (99.99%) were purchased from Sigma-Aldrich and used without further modification. Ammonium hydroxide (ACS) was purchased from ACP Chemicals Inc. Chlorin e6 (Ce6) was purchased from Frontier Scientific. Alendronate sodium trihydrate (97%), cerium (III) nitrate hydrate (REacton, 99.998%), terbium (III) nitrate hydrate (REO, 99.9%) and N-hydroxysuccinimide (NHS, >98%) were purchased from Alfa Aesar. mPEG-succinimidyl valerate (mPEG2000-SVA, MW 2000) was purchased from Laysan Bio Inc.

Citrate stabilized, doped lanthanum fluoride core/shell nanoparticles were synthesized using a slightly modified version of a previously published hydrothermal method. Briefly, citric acid (10.4 mmol) was dissolved in 35 mL of milli-Q water, and the pH adjusted to 4.5 using 28% NH_4OH. This solution was heated to 75 °C while stirring at 600 rpm. The lanthanide precursor solution (total of 1.33 mmol in 2 mL methanol) and NH4F (8.38 mmol in 2 mL water) were then added consecutively to the citric acid solution at 4 mL/h. This solution was stirred at 75 °C for 2 hours, followed by dropwise addition of lanthanum nitrate (1.33 mmol in 2 mL methanol) at 4 mL/h to form a nominally undoped LaF3 shell. After stirring for another 2 h, the mixture was cooled to room temperature and the nanoparticles were precipitated using an equal volume of ethanol followed by centrifugation at 4000 rpm for 10 min. This was repeated twice. Finally, the particles were re-suspended in distilled water and filtered through a two stage Millex 0.45/1.0 μm PVDF/APFB syringe filter to produce a final stock solution of 20-30 mg/mL.

2.2 Time-Resolved Fluorescence Measurements

Fluorescence lifetimes were measured using the time-correlated single photon counting (TCSPC) technique with the apparatus previously described[1]. Briefly, the output of a Coherent RegA 9050 Ti/sapphire regenerative amplifier (800 nm, 80 fs pulses at 250 kHz repetition rate) was coupled into an OPA (Coherent 9450) producing 504 nm pulses. The OPA output was used to generate a 252 nm ($\Delta\lambda_{HWHM} = 2$ nm) second harmonic in a type I BBO crystal. The harmonic was separated from 504 nm light by means of a calcium-fluoride prism pair. The 252 nm beam was gently focused inside the sample with focal spot of 0.8 mm diameter. The excitation power at the sample was varied between 7 – 170 μW. The photoluminescence was collected with a 3.5 cm focal length lens at 90 degrees to the excitation beam and focused by a 10 cm focal length lens into a vertical slit of a CVI CMSP112 double spectrograph with a 1/8 m total path length in

negative dispersive mode with a pair of 1200 (blazed for 200 nm) or 600 (blazed for 600 nm) grooves per mm gratings (overall *f* number 3.9). The slit widths were 1.2 mm and based on a monochromator dispersion of 14 nm mm^{-1}, provided 5 to 10 nm resolution depending on the wavelength. A Hamamatsu RU3809 microchannel plate photomultiplier was mounted on the monochromator output. A Becker and Hickl SPC-630 photon counting board was used to record the time-resolved emission. The reference signal was provided by a portion of the amplifier output sent to a fast photodiode. Count rates were held at less than 1% of the laser repetition rate to avoid pulse pile up. Typical acquisition times were 10 minutes for a single scan, but in some cases varied up to 20 minutes. Lifetimes of wavelengths higher than 400 nm were recorded with 420 nm cutoff filter to eliminate monochromator second order grating transmission. The full width at half-maximum of the instrument response function (IRF) measured from scatter off a solution of dilute coffee creamer was less than 40 ps. IRF deconvolution, multi-exponential decay fits and intensity-weighted average lifetime calculations were performed using FluoFit 4.0 software (PicoQuant, Berlin). Goodness-of-fit data and residuals were used to gauge fit results; a χ^2 between 0.9–1.5 and random distribution of residuals along the time delay axis were considered signs of accurate fitting. Lifetime decay contributions were weighted by fractional intensity. Negative amplitude decays (representing the rise times) were included in the calculation of average values, but not for fractional decay intensities. Multi-exponential decay fits were obtained from

$$I(\mathrm{t}) = \int_{-\infty}^{t} F(\mathrm{t}') \sum_{j=1}^{n} A_j e^{-\frac{t-t'}{T_j}} dt', \qquad (0.1)$$

where $F(\mathrm{t}')$ is the instrument response function, maximum n was 4.

2.3 Steady-State Fluorescence Measurements

Steady-state fluorescence was collected using a Horiba Fluorolog-3 fluorimeter. For all measurements, the emission and detection slits were set to 4 nm. Integration time was 0.1 seconds, and 5 consequent scans were collected and averaged. All spectra were corrected for variations in excitation lamp intensity. Background scans with emission of a cell with water only were also collected and when necessary subtracted from sample spectra. For samples that emitted both the UV and visible, two scans were performed separately: one for 200 – 450 nm and another one for 460 – 900 nm with a 490 nm cut off filter to block second order monochromator grating transmission. Fits to spectra were performed using a set of no more than four Gaussian functions in the Matlab Curve Fitting Toolbox with no constraints on the parameters.

2.4 Radioluminescence Measurements

Radioluminescence (scintillation) was measured using a custom built apparatus described elsewhere[2]. Briefly, a cell with nanoparticles was placed inside an x-ray machine (X-RAD iR160), which was operated at 150 kVp and 20 mA using a 2 mm Al filter. Radioluminescence was collected from the surface layer of the liquid perpendicular to X-ray direction and focused by a lens into an optical fiber. The fiber was coupled to a monochromator (CM110, Spectral Products) with overall resolution about 7 nm. The signal was detected at the monochromator output by a PMT (R928P, Hamamatsu) operating at 1 kV and subsequently processed by a photon counter (SR400, Stanford Research Systems). Obtained spectra were not corrected for monochromator and fiber transmittance and PMT sensitivity. The detector was cooled with dry ice; dark current was around 1-2 counts per second. Several measurements were done using the fiber and lens alone, an empty quartz cell, and a cell with H_2O to estimate the background radioluminescence. Solutions of nanoparticles or conjugates were measured in quartz cuvettes (Starna) at room temperature. Samples were not deoxygenated. Samples containing conjugated Chlorin e6 or Rose Bengal were replaced with fresh solutions every 20 minutes to ensure chemical stability of the sample. Concentrations of all samples we kept at 50 μg/mL or lower to avoid possible aggregation. The concentration of the nanoparticles was 22 mg/mL.

2.5 Cell Culture and Toxicity Assays

B16 murine melanoma cells were a gift of J. Teodoro, McGill Cancer Centre, and were maintained at 37 °C/5% CO2 in Dulbecco's Modified Eagle's Medium (DMEM) supplemented with 10% fetal bovine serum (FBS) and 1% penicillin/streptomycin. All cells were grown in T25 flasks and passaged every two days.

The effect of varying concentrations of rose bengal conjugates on B16 cells compared to rose bengal alone was investigated using a sulforhodamine-B (SRB) assay. In each experiment, 5000 B16 cells were plated in a 96-well plate,

except for the outermost wells, which had only PBS. After 24 hours, the wells were washed with PBS and nanoparticle conjugates with concentrations ranging from 0 to 1000 ug/mL were added. This corresponded to rose bengal concentrations from 0 to 37.6 uM. There were three wells with nanoparticle conjugates, and three wells with equivalent concentrations of rose bengal alone. The cells were incubated with nanoparticles for 2 h, after which they were washed three times with PBS and fresh DMEM added. After a further 24 hours, the cells were fixed and stained with the SRB dye, and the absorbance measured at 510 nm using a Tecan Infinite PRO 200 spectrometer.

3. RESULTS

3.1 Steady-state emission

Steady-state fluorescence quenching due to conjugated photosensitizers was observed. The UV and visible emission of the $La_{0.9}Ce_{0.1}F_3$-PEG nanoparticles and of Chlorin e6 conjugates emission spectra excited with 252 nm is shown in **Fig. 1**. A control sample that had Chlorin e6 attached to Ce-free nanoparticles also was studied to ensure that the observed quenching was due to energy transfer and not simply the presence of the nanoparticle.

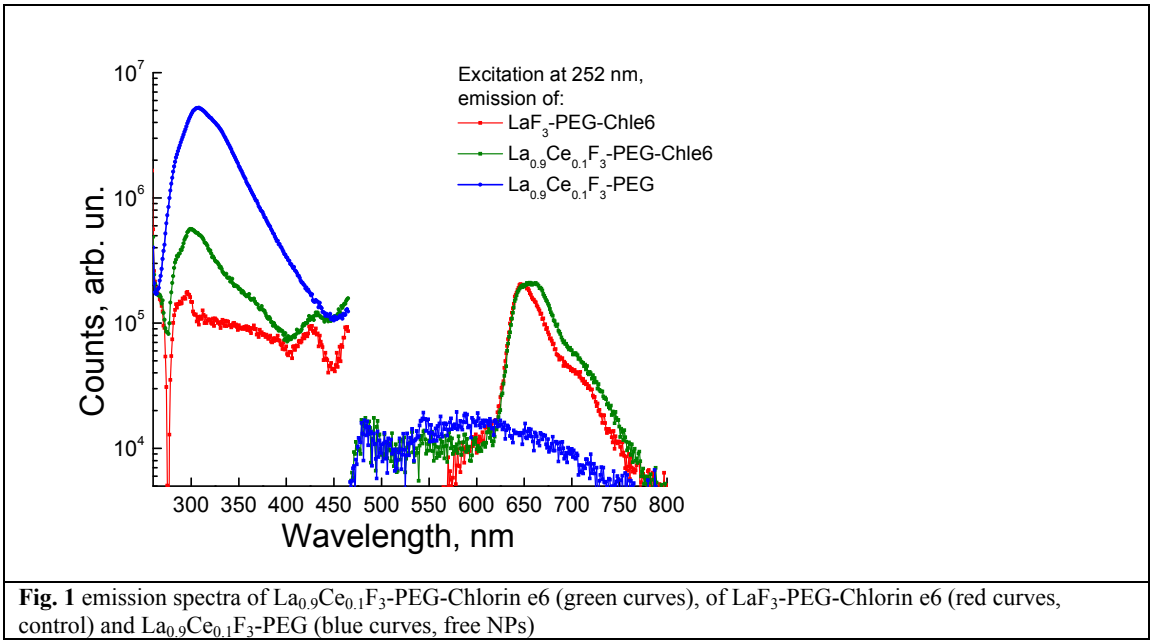

Fig. 1 emission spectra of $La_{0.9}Ce_{0.1}F_3$-PEG-Chlorin e6 (green curves), of LaF_3-PEG-Chlorin e6 (red curves, control) and $La_{0.9}Ce_{0.1}F_3$-PEG (blue curves, free NPs)

The emission of conjugated Chlorin e6 was 42% (by number of photons) more intense compared to emission of Chlorin e6 bound to Ce-free nanoparticles. At the same time the intensity of Ce ion emission (in the UV part of the spectrum) in nanoparticles that had Chlorin e6 attached was reduced by 87%.

Similar results were observed for (Ce, Tb)-doped nanoparticles with Rose Bengal covalently attached. The UV and visible parts of the $La_{0.6}Ce_{0.2}Tb_{0.2}F_3$-PEG nanoparticle emission spectra are shown in **Fig. 2**. The UV emission of $La_{0.6}Ce_{0.2}Tb_{0.2}F_3$-PEG has one very wide peak centered at 330 nm, which rises from 275 nm and extends until ~450 nm. The visible part of the $La_{0.6}Ce_{0.2}Tb_{0.2}F_3$-PEG fluorescence has 4 distinct Tb transitions located at 488 nm, 543 nm, 583 nm, and 620 nm.

Conjugation of rose bengal to the nanoparticles led to a decrease in the absolute intensity of Ce and Tb emission, suggesting energy transfer. In the UV range, Ce emission was quenched by 90%; in the visible range, Tb

emission was quenched by about 99.6% based upon the integrated number of photons detected. The emission intensity of rose bengal did not significantly change upon conjugation.

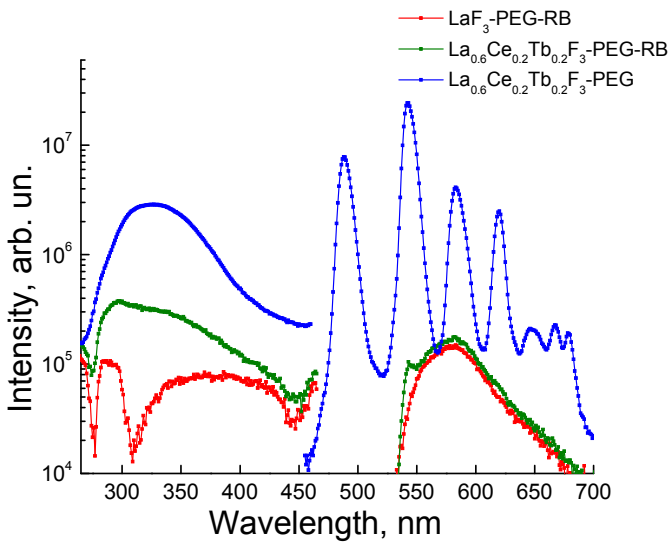

Fig. 2 Emission spectra of $La_{0.6}Ce_{0.2}Tb_{0.2}F_3$-PEG (blue curve), $La_{0.6}Ce_{0.2}Tb_{0.2}F_3$-PEG-RB (green curve) and LaF_3-PEG-RB control (red curve).

The UV part of the spectrum of $La_{0.6}Ce_{0.2}Tb_{0.2}F_3$-PEG was fitted with sum of Gaussians to identify distinct emission bands (**Fig. 3**). A satisfactory R^2 was obtained only with the sum of 4 Gaussians. Two of these bands corresponded to native D -> F Ce^{3+} transitions: G_1 and G_2 with peaks at 283 nm (4.38 $\pm$ 0.01 eV) and 305 nm (4.06 $\pm$ 0.01 eV). Bands G_3 and G_4 were attributed to perturbed Ce sites. Taking into account the small size of NPs it is reasonable that emission from the perturbed sites dominates unperturbed Ce transitions.

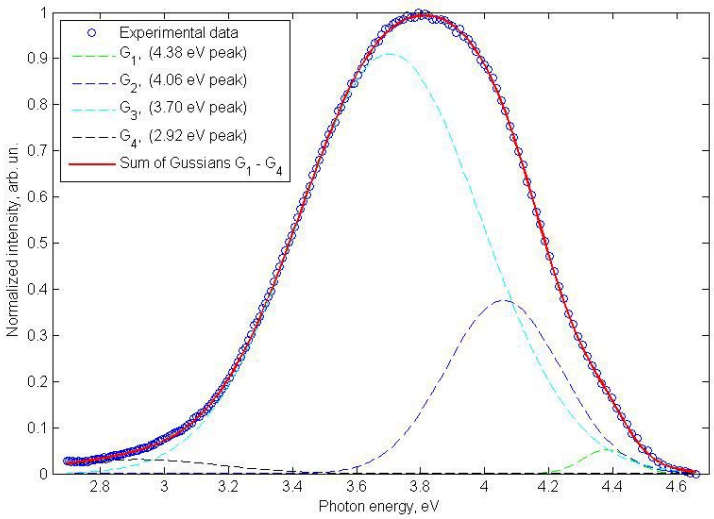

Fig. 3 UV part of $La_{0.6}Ce_{0.2}Tb_{0.2}F_3$-PEG fluorescence fitted with 4 Gaussians.

3.2 Time-resolved emission

Based on the steady-state fits, TSCPC lifetime measurements were done at 4.38 eV (283 nm), 4.15 eV (298 nm) and 4.35 eV (370 nm). The lifetimes of rose bengal were measured at 568 nm, which is close to the rose bengal emission peak and falls between the sharp Tb emission peaks. The lifetimes of the Ce emission upon conjugation to rose bengal were consistently shorter compared to nanoparticles without rose bengal. The emission lifetime of free rose bengal was a 0.09 ns monoexponential decay. Conjugated rose rengal dye had several components of the decay with lifetimes of 0.05, 0.12, 1.54 and 4.68 ns. **Figures 4 and 5** show lifetimes of Ce ions in La0.6Ce0.2Tb0.2F_3-PEG nanoparticles and in La0.6Ce0.2Tb0.2F_3-PEG-RB conjugates showing a pronounced change of the 298 and 370 nm emission lifetimes after attaching rose bengal.

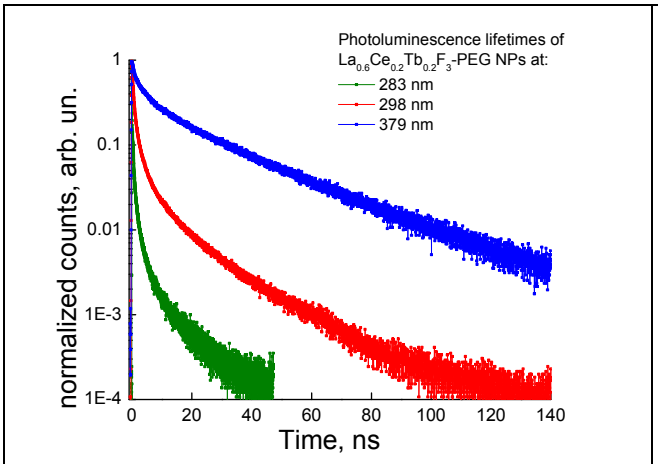

Fig. 4. Fluorescence lifetimes of $La_{0.6}Ce_{0.2}Tb_{0.2}F_3$-PEG nanoparticles at different wavelengths: 283, 298 and 379 nm.

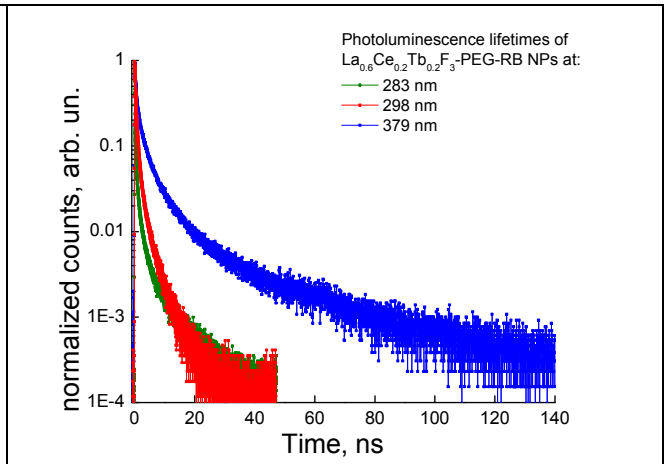

Fig. 5. Fluorescence lifetimes of $La_{0.6}Ce_{0.2}Tb_{0.2}F_3$-PEG-RB conjugates at the same as on fig. 4 (283, 298 and 379 nm) wavelengths.

Fig. 6 presents the 283 nm lifetimes before and after the conjugation procedure, and lifetimes of conjugated and free rose bengal are shown in **Fig. 7**.

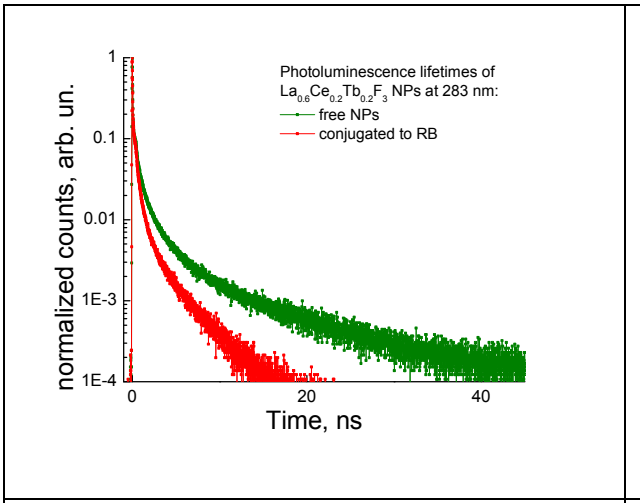

Fig. 6 Fluorescence lifetimes of free and conjugated nanoparticles at 283 nm.

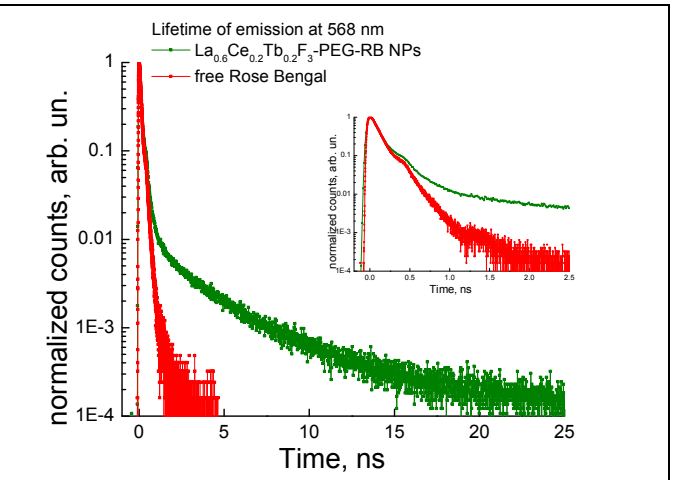

Fig. 7 Lifetimes of conjugated and free Rose Bengal. Insert shows lifetimes in the region from 0 to 2.5 ns.

3.3 Radioluminescence

The radioluminescence spectrum of $La_{0.6}Ce_{0.2}Tb_{0.2}F_3$-PEG did not significantly differ from photoexcited fluorescence, as seen in **Fig. 8**. We also attempted to detect scintillation of $La_{0.6}Ce_{0.2}Tb_{0.2}F_3$-PEG-RB conjugates, but the signal did not substantially differ from background due to very strong quenching (**Fig. 9**).

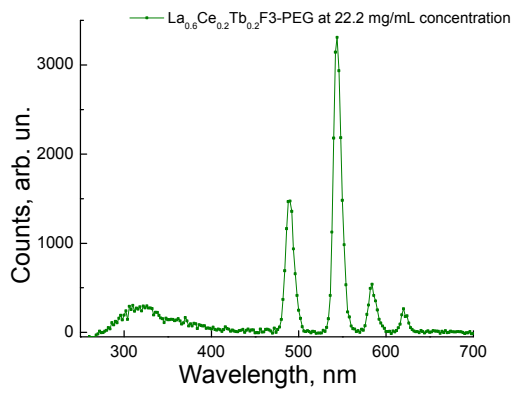

Fig 8 scintillation of $La_{0.6}Ce_{0.2}Tb_{0.2}F_3$-PEG at 22.2 mg/mL concentration

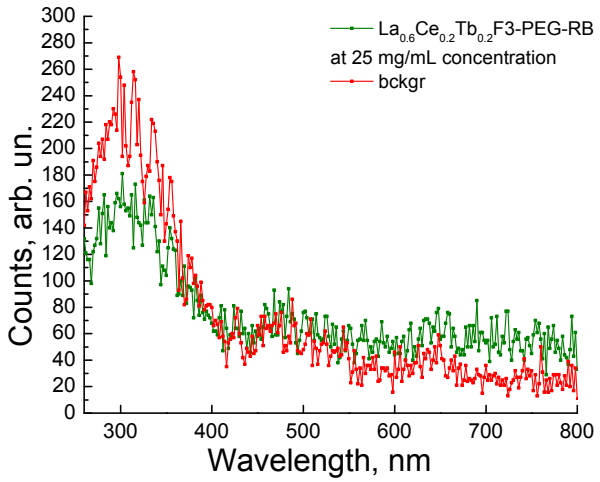

Fig. 9 $La_{0.6}Ce_{0.2}Tb_{0.2}F_3$-PEG-RB at 25 mg/mL concentration

3.4 Conjugate toxicity in cells

As initially prepared, the rose bengal-nanoparticle conjugates showed unacceptable levels of toxicity (**Fig. 10 A**). Only after ethanol wash was toxicity reduced to the level of rose bengal alone (**Fig. 10 B**). The effects of these particles in cells with radiation remain to be tested.

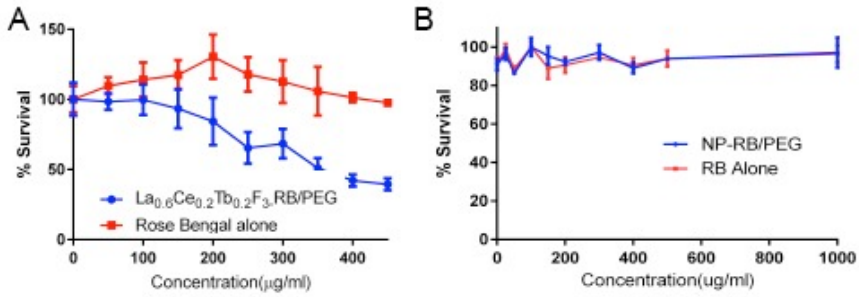

Figure 10. Survival curves of (A) Nanoparticle-rose bengal conjugates as prepared vs. rose bengal alone. (B) After 2x ethanol wash.

4. SUMMARY AND CONCLUSION

Radioluminescence spectra of $La_{0.6}Ce_{0.2}Tb_{0.2}F_3$-PEG nanoparticles are similar to the photoexcited fluorescence.

The photophysical results on the nanoparticle-rose bengal conjugates suggest that they should be useful for radiosensitization in cells. The increase of the fluorescence lifetime of conjugated rose bengal suggests energy transfer

between nanoparticles and the photosensitizer. The decreased fluorescence lifetime of the UV part of the emission spectrum of nanoparticles suggests that the excitation of rose bengal is transferred not only from Tb ions—whose emission spectra overlap with absorption spectrum of rose bengal—but also from Ce ions.

Since both Ce and Tb ions contribute to energy transfer from nanoparticle to conjugated photosensitizer it would be interesting to evaluate how elemental and fractional compositions of nanoparticle influence radioluminescence spectra shape and absolute photon yield.

Biological experiments remain to be done, and should be performed using clonogenic assays.

REFERENCES

[1] W. Ngwa, R. Kumar, S. Sridhar *et al.*, "Targeted radiotherapy with gold nanoparticles: current status and future perspectives," Nanomedicine, 9(7), 1063-1082 (2014).

[2] J. M. Kinsella, R. E. Jimenez, P. P. Karmali *et al.*, "X-ray computed tomography imaging of breast cancer by using targeted peptide-labeled bismuth sulfide nanoparticles," Angew Chem Int Ed Engl, 50(51), 12308-11 (2011).

[3] M. K. Leung, J. C. Chow, B. D. Chithrani *et al.*, "Irradiation of gold nanoparticles by x-rays: Monte Carlo simulation of dose enhancements and the spatial properties of the secondary electrons production," Med Phys, 38(2), 624-31 (2011).

[4] F. Van den Heuvel, J. P. Locquet, and S. Nuyts, "Beam energy considerations for gold nano-particle enhanced radiation treatment," Phys Med Biol, 55(16), 4509-20 (2010).

[5] C. Alric, I. Miladi, D. Kryza *et al.*, "The biodistribution of gold nanoparticles designed for renal clearance," Nanoscale, 5(13), 5930-9 (2013).

[6] R. Cao-Milan, and L. M. Liz-Marzan, "Gold nanoparticle conjugates: recent advances toward clinical applications," Expert Opinion on Drug Delivery, 11(5), 741-752 (2014).

[7] J. Lee, D. K. Chatterjee, M. H. Lee *et al.*, "Gold nanoparticles in breast cancer treatment: Promise and potential pitfalls," Cancer Letters, 347(1), 46-53 (2014).

[8] X. H. Huang, X. H. Peng, Y. Q. Wang *et al.*, "A Reexamination of Active and Passive Tumor Targeting by Using Rod-Shaped Gold Nanocrystals and Covalently Conjugated Peptide Ligands (vol 4, pg 5887, 2010)," Acs Nano, 5(8), 6765-6765 (2011).

[9] A. K. Iyer, G. Khaled, J. Fang *et al.*, "Exploiting the enhanced permeability and retention effect for tumor targeting," Drug Discovery Today, 11(17-18), 812-818 (2006).

[10] B. B. Cerqueira, A. Lasham, A. N. Shelling *et al.*, "Nanoparticle therapeutics: Technologies and methods for overcoming cancer," Eur J Pharm Biopharm, 97(Pt A), 140-51 (2015).

[11] J. T. Duskey, and K. G. Rice, "Nanoparticle ligand presentation for targeting solid tumors," AAPS PharmSciTech, 15(5), 1345-54 (2014).

[12] R. R. Allison, "Photodynamic therapy: oncologic horizons," Future Oncol, 10(1), 123-4 (2014).

[13] E. J. Sanchez-Barcelo, and M. D. Mediavilla, "Recent patents on light based therapies: photodynamic therapy, photothermal therapy and photoimmunotherapy," Recent Pat Endocr Metab Immune Drug Discov, 8(1), 1-8 (2014).

[14] A. M. Rkein, and D. M. Ozog, "Photodynamic therapy," Dermatol Clin, 32(3), 415-25, x (2014).

[15] W. Chen, and J. Zhang, "Using Nanoparticles to Enable Simultaneous Radiation and Photodynamic Therapies for Cancer Treatment," Journal of Nanoscience and Nanotechnology, 6(4), 1159-1166 (2006).

[16] Y. Liu, W. Chen, S. Wang *et al.*, "Investigation of water-soluble x-ray luminescence nanoparticles for photodynamic activation," Applied Physics Letters, 92(4), 043901 (2008).

[17] H. Guo, H. Qian, N. M. Idris *et al.*, "Singlet oxygen-induced apoptosis of cancer cells using upconversion fluorescent nanoparticles as a carrier of photosensitizer," Nanomedicine: Nanotechnology, Biology and Medicine, 6(3), 486-495 (2010).

[18] D. R. Cooper, K. Kudinov, P. Tyagi *et al.*, "Photoluminescence of cerium fluoride and cerium-doped lanthanum fluoride nanoparticles and investigation of energy transfer to photosensitizer molecules," Physical Chemistry Chemical Physics, 16(24), 12441-12453 (2014).